Synthesis of mesoporous copper oxide microspheres with different surface areas and their lithium storage properties

Zailei Zhang [a,b], Han Chen [a,*], Xilin She [b], Jin Sun [b], Jaclyn Teo [c], Fabing Su [a,*]

[a] State Key Laboratory of Multiphase Complex Systems, Institute of Process Engineering, Chinese Academy of Sciences, Beijing 100190, China
[b] College of Chemical and Environmental Engineering, Qingdao University, Qingdao 266071, China
[c] Institute of Chemical Engineering and Sciences, A*star, 1 Pesek Road, Jurong Island, Singapore 627833, Singapore

HIGHLIGHTS

► Mesoporous copper oxide microspheres with different surface areas were prepared.
► Mesoporous copper oxides with high surface area show improved anode properties.
► Developed pore structure causes more accommodation and fast diffusion for Li ions.

ARTICLE INFO

ABSTRACT

We report the comparative investigation on the electrochemical application of mesoporous copper oxide (Cu_2O and CuO) microspheres with different surface areas as anode materials in Li-ion batteries. Mesoporous Cu_2O microspheres with a narrow particle size distribution are synthesized by a hydrothermal method and CuO is obtained by subsequent oxidation of Cu_2O. The synthesized mesoporous Cu_2O and CuO microspheres possess a surface area of 12.7–65.8 and 5.2–37.6 $m^2 \, g^{-1}$ and an average crystal size of 15.0–20.5 and 10.4–15.9 nm, respectively. The result reveals that the mesoporous Cu_2O and CuO microspheres with a higher surface area show a higher capacity and better cyclability than those with a lower surface area. The mesoporous Cu_2O and CuO microspheres with a surface area of 65.8 and 37.6 $m^2 \, g^{-1}$ show an initial charge capacity of 430.5 mAh g^{-1} and 601.6 mAh g^{-1} and deliver a capacity as high as 355.2 mAh g^{-1} and 569.8 mAh g^{-1} at 0.1 C after 50 cycles, respectively. This is because the highly developed mesoporous structure can enhance the accommodation of lithium ions, shorten the diffusion distance for lithium ions, and increase the absorption of electrolyte.

© 2012 Elsevier B.V. All rights reserved.

1. Introduction

Li-ion batteries (LIBs) currently are the dominant power sources for portable appliances including mobile phones, notebook computers, and electric vehicles [1–4]. Transition-metal oxides (TMOs, here TM = Co, Fe, Ni, Cu, etc.) have demonstrated to be promising high-performance materials for the next generation of LIBs because of their much higher lithium storage capacities than that of commercially used graphite (372 mAh g^{-1}), as well as their safer nature, environmental benignity, and low cost [5–7]. The mechanism for lithium storage in TMOs is mainly based on a heterogeneous conversion reaction: $2Li + TMO \rightarrow Li_2O + TM$, which involves the formation and decomposition of Li_2O via the reduction and oxidation of metal nanoparticles [5]. This reaction

depends on the lattice structure and dimensional scale of metal oxides, thermodynamic and kinetic conditions, as well as the current rates [8], in contrast to the classical Li insertion/desertion or Li-alloying processes. Recently, many nanostructured TMO materials have been developed for Li-ion batteries, such as needle-like Co_3O_4 nanotubes [9], Fe_3O_4-based Cu nano-architectured electrode [10], α-Fe_2O_3 hollow spheres [11], α-MoO_3 nanorods [12], hierarchically nanostructured composite of MnO_2/conjugated polymer/graphene [13], NiO nanocone array [14], core–shell structure Cu_2O [15], and CuO thin films [16]. More recently, porous TMO materials, such as mesoporous Co_3O_4 [17,18], mesoporous CoO@C [19], ordered mesoporous MnO_2 [20], mesoporous TiO_2–C nanosphere [21], and mesoporous crystalline TiO_2/carbon composites [22] have been reported to exhibit better electrochemical performance than bulk materials. This is due to their large surface areas and mesoporous structures, which could accommodate more Li ions, permit more facile transport of Li ions in the electrolyte within the pores and

---

* Corresponding authors. Tel.: +86 10 82544850; fax: +86 10 82544851.
E-mail addresses: lzdxn@yahoo.com.cn (H. Chen), fbsu@mail.ipe.ac.cn (F. Su).

across the electrode/electrolyte interface, as well as enhance the diffusion of Li ions within the electrode.

Among the TMO materials, copper oxides such as CuO and Cu_2O have attracted increased attention because of their superiorities in properties such as a high theoretical capacity (670 mAh g^{-1} for CuO) and improved safety compared to graphite. When used as an anode material, a conversion mechanism for CuO is expected as follows: $CuO + 2Li^+ \leftrightarrow Li_2O + Cu - 2e^-$. Guan et al. [23] found that the first discharge and charge capacities of CuO hollow spheres are higher than those of CuO solid spheres because of the synergetic effect that exists due to the small diffusion lengths in the building blocks of nanorods, and a proper void space, that effectively buffers the volume expansion. Xiang et al. [24] reported the discharge capacities and cycling performance of dandelion-like and caddice clew-like CuO are much better than that of leaf-shaped and shuttle-shaped CuO due to the large contact area for CuO/electrolyte. Morales et al. [16] found the CuO film constructed with the smallest grain size exhibited an excellent electrochemical response and sustained a specific capacity. Numerous reports reveal that the electrochemical performance of CuO can be enhanced with a nanostructured morphology [25−27], a formation of CuO film [16], and with a hybrid composition [28,29]. Although the capacity of Cu_2O (375 mAh g^{-1}) is not higher than that of CuO, when used as an anode material for Li-ion batteries, many efforts have been undertaken to explore the improvement of its electrochemical performance because the use of carbonaceous anode materials in LIBs leads to the risk of safety problems when operating under high current densities. Bijani et al. [30] found that the thinner Cu_2O film exhibited the good electrochemical performance. Zhang et al. [31] demonstrated cubic Cu_2O particles delivered a higher reversible discharge capacity and better cyclability than the star-shaped Cu_2O. Fu et al. [15] found that a better crystallinity of Cu_2O materials led to a larger discharge capacity and a smaller particle size results in higher columbic efficiency and larger reversible capacity. The published work demonstrated that the electrochemical performance of Cu_2O can be improved by optimizing their morphologies [31], crystallinity and particle size [15], and the composition [32,33].

Previous work of Tarascon and co-workers systematically explored the particle size effects of copper oxides (CuO and Cu_2O) on their electrochemical performance toward lithium [34], and they found that the capacity of copper oxide-based Li-cells upon cycling was strongly dependent on the particle size. Herein, we reported the study of the electrochemical properties of mesoporous copper oxide microspheres (Cu_2O and CuO) with different surface areas, when they are used as anode materials in Li-ion batteries. Mesoporous Cu_2O microspheres with a narrow particle size distribution were synthesized by hydrothermal method and CuO was obtained by subsequent oxidation of Cu_2O. Our experimental result reveals that the mesoporous Cu_2O and CuO microspheres with a higher surface area show a higher capacity and better cyclability than those with a lower surface area.

2. Experimental

2.1. Material synthesis

All the reagents were of analytical grade and purchased from Sinopharm Chemical Reagent Co., Ltd. Cu_2O microspheres were prepared with a hydrothermal method [35] and the synthesis conditions are shown in Table 1. In a typical synthesis (Cu_2O-1 In Table 1), 1.0 g of copper acetate ($Cu(CH_3COO)_2 \cdot H_2O$) was dissolved in a mixture of 10.0 mL of deionized water with 50.0 mL absolute alcohol (CH_3CH_2OH) and 20.0 mL glycol ($C_2H_6O_2$) to form a solution in a beaker, and the solution is then heated to 70 °C under stirring, after which 1.4 g of sodium hydroxide (NaOH) and 1.2 g of glucose ($C_6H_{12}O_6 \cdot H_2O$) were added. After stirring for another 30 min at 70 °C, the products were cooled down to room temperature. The resulting precipitate was collected by centrifugation, and washed with distilled water and absolute ethanol, and then finally dried in vacuum at 60 °C for 8 h (named Cu_2O-1, Cu_2O-2, and Cu_2O-3). CuO microspheres were synthesized by calcining Cu_2O-1, Cu_2O-2, and Cu_2O-3 at 350 °C for 6 h in air, and named as CuO-1, CuO-2, and CuO-3, respectively.

2.1.1. Characterization

The porous nature of the samples was investigated using physical adsorption of nitrogen at liquid-nitrogen temperature (−196 °C) on an automatic volumetric sorption analyzer (NOVA3200e, Quantachrome). Prior to the measurement, the sample was degassed at 200 °C for 5 h under vacuum. The specific surface areas were determined according to the Brunauer-Emmett-Teller (BET) method in the relative pressure range of 0.05−0.2. Pore size distribution (PSD) curves were derived from the Barrett-Joyner-Halenda (BJH) method using the adsorption branches. The pore sizes were estimated from the maximum positions of the BJH PSD curves. X-ray diffraction patterns (XRD) were recorded on a PANalytical X'Pert PRO MPD using the Kα radiation of Cu ($\lambda = 1.5418$ Å). The Particle size distribution was measured by Laser Particle Size Analyzer (BT-9300Z, Bettersize Instruments Ltd., China). The microscopic feature of the as-synthesized powders was characterized by field-emission scanning electron microscopy (SEM) (JSM-6700F, JEOL, Tokyo, Japan) and high-resolution transmission electron microscopy (HRTEM) (JEM-2010F, JEOL, Tokyo, Japan). Thermal gravimetric (TG) analysis was carried out on an EXSTAR TG/DTA 6300 (Seiko Instruments, Japan) using a heating rate of 5 °C min^{-1} in air (200 mL min^{-1}). Temperature programmed reduction (TPR) measurements were carried out on Automated chemisorption analyzer (ChemBET pulsar TPR/TPD, Quantachrome). For this analysis, 0.10 g of Cu_2O (and CuO) microspheres was loaded in a quartz U-tube. Prior to the measurement, the sample was degassed at 200 °C for 30 min under helium. When the temperature dropped to 20 °C, the gas was changed to 9.9% H_2/Ar. Finally, the sample was heated from 20 °C to 800 °C at 10 °C min^{-1} under the flow of 9.9% H_2/Ar at 30 mL min^{-1}.

2.2. Electrochemical measurement

The working electrode was prepared by mixing the Cu_2O or CuO active materials, acetylene black, and polyvinylidene fluoride (PVDF) in a weight ratio of 75:15:10 with N-methylpyrrolidone (NMP) as a solvent. The resulting slurries were cast onto copper current collectors, and then dried at 120 °C under vacuum for 12 h. The foils were rolled into 30 μm thin sheets, and then cut into disks which are 14 mm in diameter. CR2016 coin-type cells were assembled in an argon-filled glove box. Lithium foils are used as the counter electrodes and polypropylene microporous films (Celgard

Table 1
The synthesis conditions used for preparing Cu_2O.

Sample	Water (mL)	Ethanol (mL)	Glycol (mL)	Copper acetate (g)	Sodium hydroxide (g)	Glucose (g)	Temperature (°C)	Time (min)
Cu_2O-1	10	50	20	1.0	1.4	1.2	70	30
Cu_2O-2	10	50	20	1.0	1.4	1.2	80	30
Cu_2O-3	10	50	20	0.5	0.7	0.6	70	30

2400) are used as separators. The liquid electrolyte is 1 mol L^{-1} $LiPF_6$ in a mixture of ethylene carbonate (EC) and dimethyl carbonate (DMC) (1:1, v/v). The galvanostatic charge and discharge tests were carried out by the CT2001A LAND testing instrument in a voltage range between 0.01 and 3.0 V at a current rate of 0.1 C (1C = 375 mA g^{-1} for Cu_2O and 1C = 674 mA g^{-1} for CuO). Cyclic voltammogram (CV) was carried out in the voltage range 0–3 V at a scanning rate of 0.1 mv s^{-1} at room temperature. Electrochemical impedance spectroscopy (EIS) measurements were conducted using a CHI660D potentiostat over a frequency range from 100 kHz to 10 mHz with an ac oscillation of 5 mV under full charge state after the first cycle.

3. Results and discussion

Fig. 1a shows the XRD patterns of the of Cu_2O and CuO micro-spheres. It can be seen that for all the Cu_2O samples, the diffraction peaks at 2θ values of 29.7, 36.7, 42.7, 61.6, and 73.5° correspond to the lattice plane of (110) (111) (200) (220), and (311), respectively, suggesting the presence of pure Cu_2O with cubic symmetry (JCPDS No. 05-0667). Calculating using the Debye-Scherrer formula based on the peak at 36.7°, the average grain (crystal) size of Cu_2O-1, Cu_2O-2, and Cu_2O-3 is 15.0, 15.8, and 20.5 nm, respectively. The diffraction peaks of CuO-1, CuO-2, and CuO-3 at 35.7, 39.0, 49.2, 61.8, 66.2, 68.4, and 75.4° correspond to the lattice plane of (−111) (111) (−202) (−113) (022) (220), and (004), respectively, indicating the presence of the pure CuO with monoclinic symmetry (JCPDS No.065-2309). The absence of Cu_2O peaks indicates that the synthesized Cu_2O microspheres were completely converted to CuO under the oxidation condition used. The average grain size of CuO-1, CuO-2, and CuO-3 is calculated to be 10.4, 12.7, and 15.9 nm based on the peak at 35.7°, respectively. Fig. 1b shows the particle size distribution curves for these samples. The median diameter of Cu_2O-1, Cu_2O-2, Cu_2O-3, CuO-1 CuO-2 and CuO-3 at the maximum peak position is 0.89, 0.95, 1.02, 1.15, 1.21 and 1.26 μm, suggesting a relatively narrow particle size distribution within all products obtained. Previous work demonstrated that the particle size and grain size of TMO materials have significant effect on their LIB properties [34,36]. Thus, both sizes of Cu_2O and CuO microspheres in our work have to be controlled within a similar level for a fair comparison. Fig. 1c shows the isotherms of mesoporous Cu_2O and CuO samples. These isotherms with a hysteresis loop in the relative pressure range of 0.4–1.0 belong to that of type-IV. Their BET surface areas are 65.8 m^2 g^{-1} for Cu_2O-1, 45.3 m^2 g^{-1} for Cu_2O-2, 12.7 m^2 g^{-1} for Cu_2O-3, 37.6 m^2 g^{-1} for CuO-1, 26.5 m^2 g^{-1} for CuO-2, and 5.2 m^2 g^{-1} for CuO-3. The PSD curves of these samples in Fig. 1d shows that the pore size at the maximum position is 26.7 nm for Cu_2O-1, 28.4 nm for Cu_2O-2, 29.1 nm for CuO-1, and 31.6 nm for CuO-2, indicating the presence of their mesoporous structure. For Cu_2O-3 and CuO-3, the pore size is around 50 nm, approaching the higher limit of the mesoporous range.

Fig. 2 shows the SEM and TEM images of mesoporous Cu_2O microspheres. It is seen that in Fig. 2a, Cu_2O-1 possesses a diameter of about 400–700 nm. These microspheres are constructed with small nanoparticles (building block units) with a size of around 10–40 nm. TEM image in Fig. 2b reveals the uniform microspheres of Cu_2O-1 with the mesoporous structure on the external surface. HRTEM image of Cu_2O-1 (inset of Fig. 2b) exhibits that a large number of nanocrystals are packed into the Cu_2O microspheres with different orientations. The lattice plane distance was
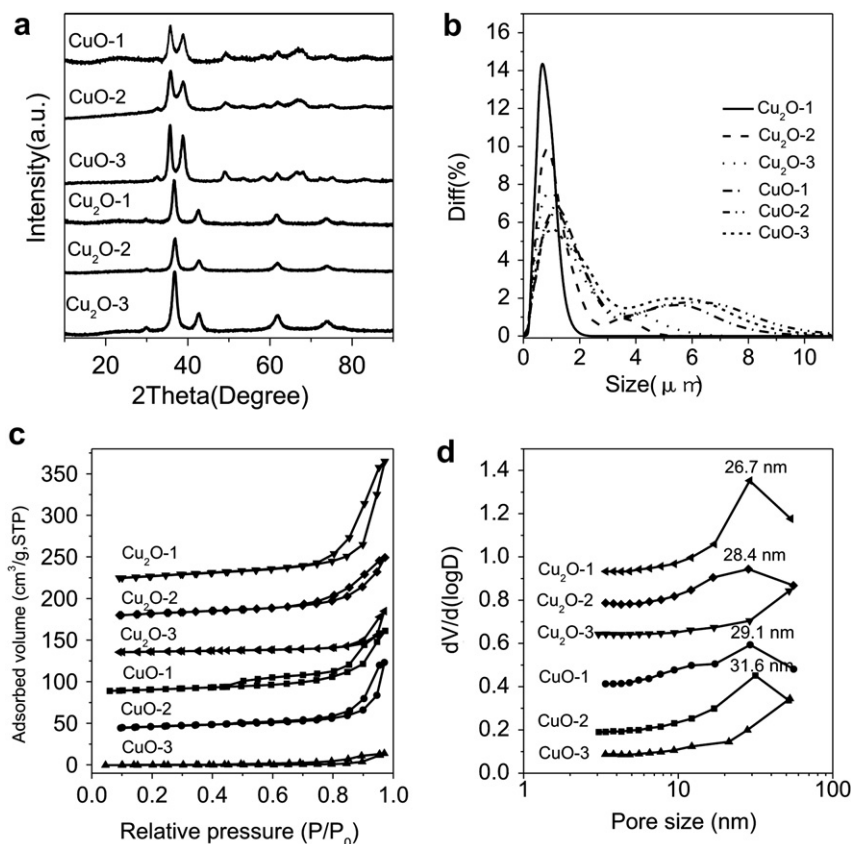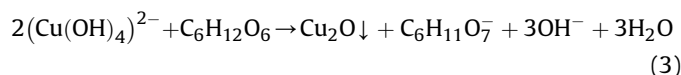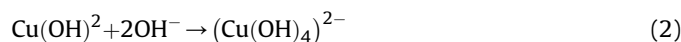

Fig. 1. XRD patterns (a), the particle size distribution curves (b), N_2 adsorption–desorption isotherms, (c) and their PSD curves (d) of all Cu_2O and CuO samples (for clarity, the isotherm of Cu_2O-2, Cu_2O-3, CuO-1, CuO-2, and CuO-3 were vertically shifted for 45, 90, 135, 180, and 225 cm^3 g^{-1}, respectively).

measured to be 0.25 nm, and this is in good agreement with the (111) plane distance of cubic Cu_2O (0.2465 nm calculated from XRD). The morphology of the sample Cu_2O-2 in Fig. 2c and its inset shows no obvious change compared with that of Cu_2O-1. The microspheres still consist of a large number of small nanoparticles with a size in tenth of nanometers. Fig. 2d and its inset reveal the morphology of Cu_2O-3 microspheres with a diameter of 300–600 nm, similar to that of Cu_2O-1. The Cu_2O microspheres formation reactions are shown in equations (1)–(3) [37,38].

$$Cu^{2+} + 2OH^- \rightarrow Cu(OH)_2\downarrow \qquad (1)$$

$$Cu(OH)^2 + 2OH^- \rightarrow (Cu(OH)_4)^{2-} \qquad (2)$$

$$2(Cu(OH)_4)^{2-} + C_6H_{12}O_6 \rightarrow Cu_2O\downarrow + C_6H_{11}O_7^- + 3OH^- + 3H_2O \qquad (3)$$

In this synthesis process, the glycol molecules absorbed on the surface of the nanoparticles acts as structure-directing agents to regulate the surface state. These small molecules on the surface influence the nucleation and aggregation process of the nano-particles, and finally this leads to the formation of mesoporous structures within the interstitial space among the stacked building block of nanoparticles, via the process of Ostwald ripening [39]. The assembling nanoparticle size and surface area of these products can be controlled by tuning the appropriate synthesis conditions.

Fig. 3a shows the SEM image of the mesoporous CuO-1 micro-spheres derived from the calcination of Cu_2O-1, in which, CuO-1 microspheres with a diameter of 400–700 nm seem to be assem-bled with small nanoparticles with a size of around 10–40 nm. TEM image for single microsphere of CuO-1 in Fig. 3b reveals its uniform mesoporous structure. Inset of Fig. 3b shows the HRTEM image on the edge of CuO-1, in which, a lattice plane distance is about

0.25 nm, consistent with the (−111) plane distance of monoclinic CuO (0.2516 nm tabulated from XRD). SEM images in Fig. 3c and d, as well as their TEM images (insets) reveal that the CuO-2 and CuO-3 microspheres have porous structure and relatively uniform morphology with a diameter of 300–800 nm. It can be concluded that the morphology and mesostructure of CuO products are retained after the calcination of Cu_2O.

Fig. 4a shows the TG curves of the Cu_2O products in air. It can be seen that the oxidation of Cu_2O-1 occurred within a narrow temperature range of about 270–370 °C. In contrast, the oxidation for Cu_2O-2 and Cu_2O-3 took place in a wide range of 220–590 °C. These may suggest that Cu_2O-1 has a relatively uniform and small grain size, as well as a large surface area, compared to that of Cu_2O-2 and Cu_2O-3, and this is in accordance with previous observation. The weight increase for these samples is consistent with the theoretical value, implying the predominance of the Cu_2O. Fig. 4b shows the H_2-TPR curves of all samples. The maximum position of the H_2 consumption peak for Cu_2O-1, Cu_2O-2, and Cu_2O-3 is located at about 240, 270, and 300 °C, respectively, while, for CuO-1, CuO-2, and CuO-3 samples, the maximum position is located at about 315, 317, and 345 °C, respectively. This indicates that the grain size of Cu_2O-1 and CuO-1 is smaller than that of other Cu_2O and CuO samples, respectively, and is consistent with the XRD results. This is because copper oxides with a small grain size are relatively easier to be reduced due to the more exposed surface area.

Fig. 5 shows the electrochemical properties of the mesoporous Cu_2O microspheres as anode materials in LIBs. Fig. 5a reveals the initial discharge and charge curves of Cu_2O electrodes at a 0.1 C rate. The initial discharge capacity of Cu_2O-1 (592.2 mAh g^{-1}) is higher than that of Cu_2O-2 (575.5 mAh g^{-1}) and Cu_2O-3 (520.9 mAh g^{-1}). The initial charge capacity of Cu_2O-1 (430.5 mAh g^{-1}) is also larger than that of Cu_2O-2 (371.1 mAh g^{-1}) and Cu_2O-3 (280.6 mAh g^{-1}), and is even higher than that of the reported cubic shape Cu_2O (390 mAh g^{-1}) [31]. The constant slopes with multiple small
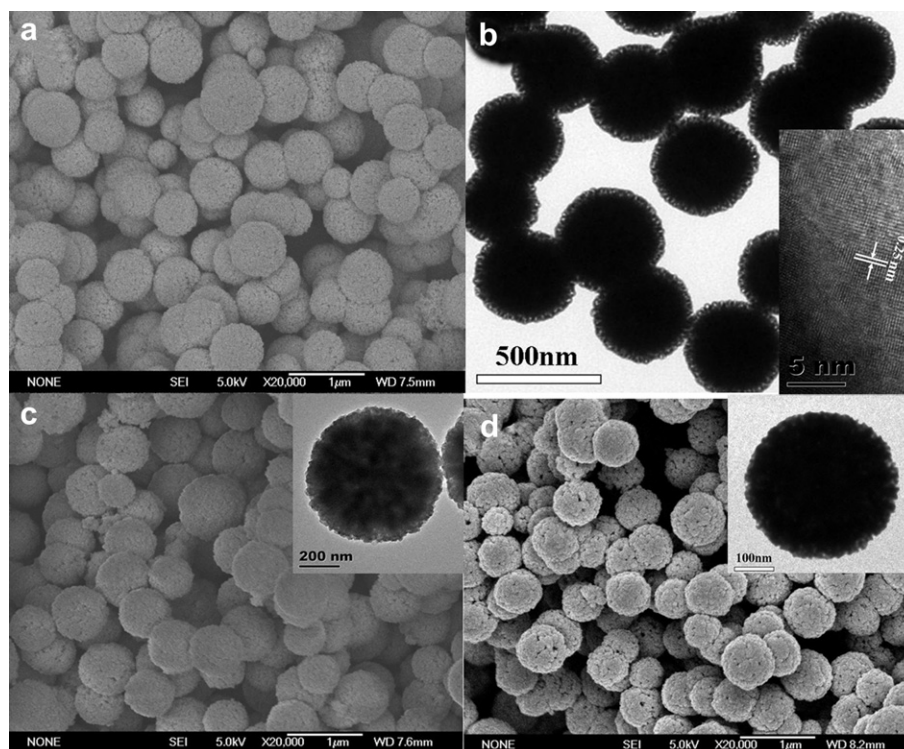

Fig. 2. SEM image of the mesoporous Cu_2O-1 (a), Cu_2O-2 (c), and Cu_2O-3 (d) (insets are their respective TEM images), together with TEM image of Cu_2O-1 (b) (inset is the HRTEM image).
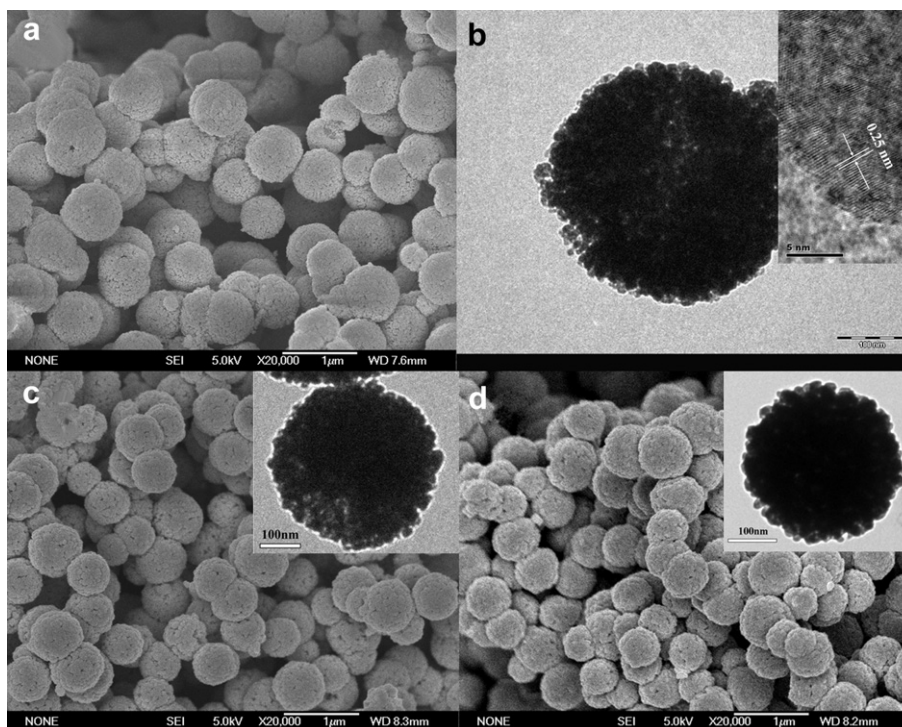
Fig. 3. SEM image of mesoporous CuO-1 (a), CuO-2 (c), and CuO-3 (d) (insets are their respective TEM images), and TEM image of CuO-1 (b) (inset is the HRTEM image).

plateaus indicate that a multi-phase transition takes place upon the conversion reaction between Cu_2O and lithium. The initial coulomb efficiency of the samples is in the order of: Cu_2O-1 (72.7%) > Cu_2O-2 (64.4%) > Cu_2O-3 (53.9%). Their capacity loss in the first cycle may be mainly ascribed to diverse irreversible processes such as the inevitable formation of solid electrolyte interface (SEI layer) and electrolyte decomposition [40], which are common for most anode materials. Fig. 5b shows the cycling performance of Cu_2O samples. The capacity of Cu_2O-1, Cu_2O-2 and Cu_2O-3 is respectively 355.2 mAh g^{-1}, 333.8 mAh g^{-1}, and 200.6 mAh g^{-1} at a scan rate of 0.1 C after 50 cycles, suggesting that Cu_2O-1, the sample with the highest surface area, possesses a largest capacity and best cyclability. The capacity of Cu_2O-1 is even higher than that of nano-structured Cu_2O thin film (350 mAh g^{-1} at 1/12 C) [30], and porous Cu_2O (336 mAh g^{-1} at 0.1 C) [41] after 50 cycles. Fig. 5c reveals the initial charge curves of mesoporous Cu_2O-1 at different rates. The charge capacity at 0.2, 0.5, and 1.0 C is 346.1, 270.7, and

184.0 mAh g^{-1}, respectively. As the capacity loss in TMO electrodes is associated with a large volume expansion, it leads to particle pulverization and agglomeration during cycling [42,43]. Fig. 5d shows that the capacity of Cu_2O-1 after 20 charge/discharge cycles is 320.6 mAh g^{-1} at 0.2 C, 205.6 mAh g^{-1} at 0.5 C, and 165.6 mAh g^{-1} at 1.0 C, further demonstrating the good cyclability of Cu_2O-1 at different scan rates. It should be pointed out that the capacity of electrodeposited Cu_2O film is only 220 mAh g^{-1} at 0.2 C [44], lower than that of Cu_2O-1 at different rates.

Fig. 5e shows the CV curves of mesoporous Cu_2O samples during the first cycle. In the first discharge process, Cu_2O-1 has three cathodic peaks located at 1.99 V (weak), 0.91 V (weak), and 0.57 V (strong), and for Cu_2O-2, the three cathodic peaks are at 1.77 V (weak), 0.74 V (strong) and 0.57 V (weak). For Cu_2O-3, only two cathodic peaks are located at 0.97 V (strong) and 0.28 V (strong). The sharp and strong peak can be ascribed to the reduction of Cu_2O to Cu matrix and formation of Li_2O [34]. However, the intensities of
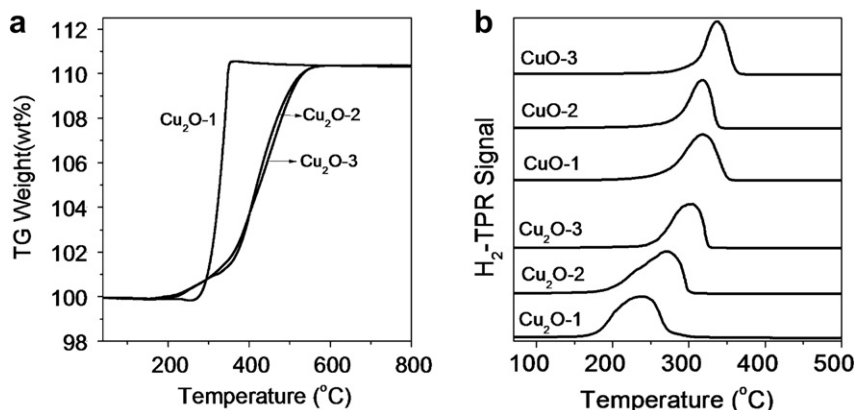

Fig. 4. TG curves of Cu_2O-1, Cu_2O-2, and Cu_2O-3 (a), and H_2-TPR curves of Cu_2O-1, Cu_2O-2, Cu_2O-3, CuO-1, CuO-2, and CuO-3 (b).
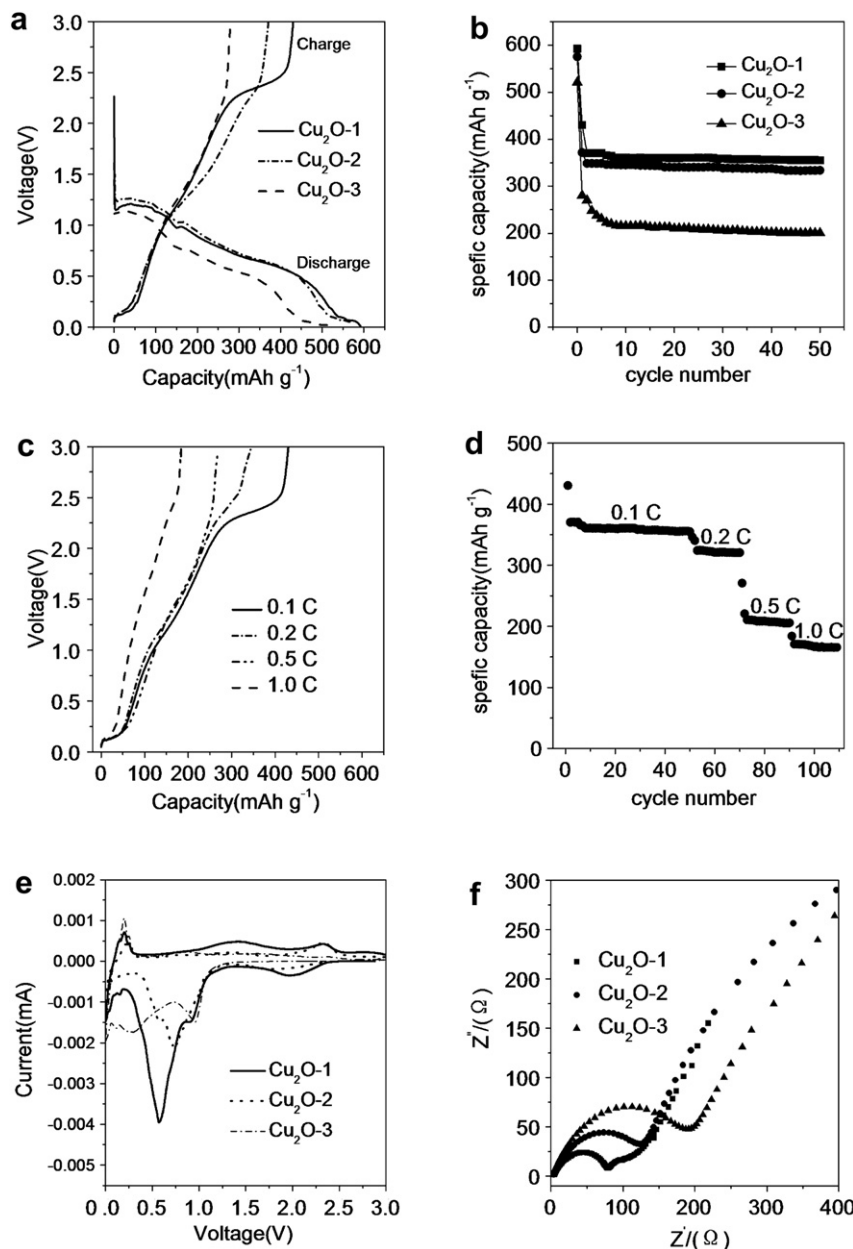
Fig. 5. Electrochemical properties of Cu$_2$O-1, Cu$_2$O-2, and Cu$_2$O-3: (a) initial charge and discharge curves and (b) cycling property between 3.0 and 0.01 V at a current density of 0.1 C, (c) The charge curves and (d) its rate performance of Cu$_2$O-1 anode at different current densities, (e) CV curves at a scan rate of 0.1 mV s^{-1}, and (f) Nyquist plots at the electrode potentials from 0.70 to 0.10 V.

both cathodic peaks for Cu$_2$O-3 are much smaller than those of Cu$_2$O-1 and Cu$_2$O-2 possibly due its lower surface area and poorer pore structure. The electrochemical impedance spectra of all the samples are shown in Fig. 5f. It shows a high-frequency semicircle, a medium-frequency semicircle, and a low-frequency inclined line, which is typically assigned to the existence of the SEI film, the charge transfer and double layer, and the lithium-diffusion process within electrodes, respectively [29,41]. It is well established that the high frequency semicircle is associated with the charge-transfer impedance on electrode/electrolyte interface [45]. Obviously, the Cu$_2$O-1 electrode shows a smaller semicircle within the high frequency, indicative of lower impedance than that of Cu$_2$O-2 and Cu$_2$O-3. This could explain the lower polarization and good rate performance of Cu$_2$O-1.

Fig. 6 shows the electrochemical properties of the CuO samples as anode materials in Li-ion batteries. In Fig. 6a, the initial discharge

capacity is 967.1 mAh g^{-1} for CuO-1, 1133.9 mAh g^{-1} for CuO-2, and 1081.2 mAh g^{-1} for CuO-3, and the initial charge capacity of CuO-1, CuO-2 and CuO-3 is 601.6, 592.3 and 382.6 mAh g^{-1} respectively. Thus, the initial coulomb efficiency of the samples is in the order of CuO-1 (62.2%) > CuO-2 (52.2%) > CuO-3 (35.4%), similar to that of the Cu$_2$O trend above. Their capacity loss in the first cycle is ascribed to diverse irreversible processes such as the inevitable formation of solid electrolyte interface (SEI layer) and electrolyte decomposition for most TMO materials. It should be mentioned that the first discharge and charge capacities of mesoporous CuO-1 microspheres are comparable to those of hollow CuO spheres (971 and 606 mAh g^{-1} at 0.1 C) [23], but it is believed that the former volume capacity should be larger than latter because of a larger internal space of the hollow structure. The cycling performance at 0.1 C in Fig. 6b shows that the capacity after 50 cycles for CuO-1, CuO-2, and CuO-3 is 569.8, 505.1, and 331.7 mAh g^{-1}, with 94.7%,
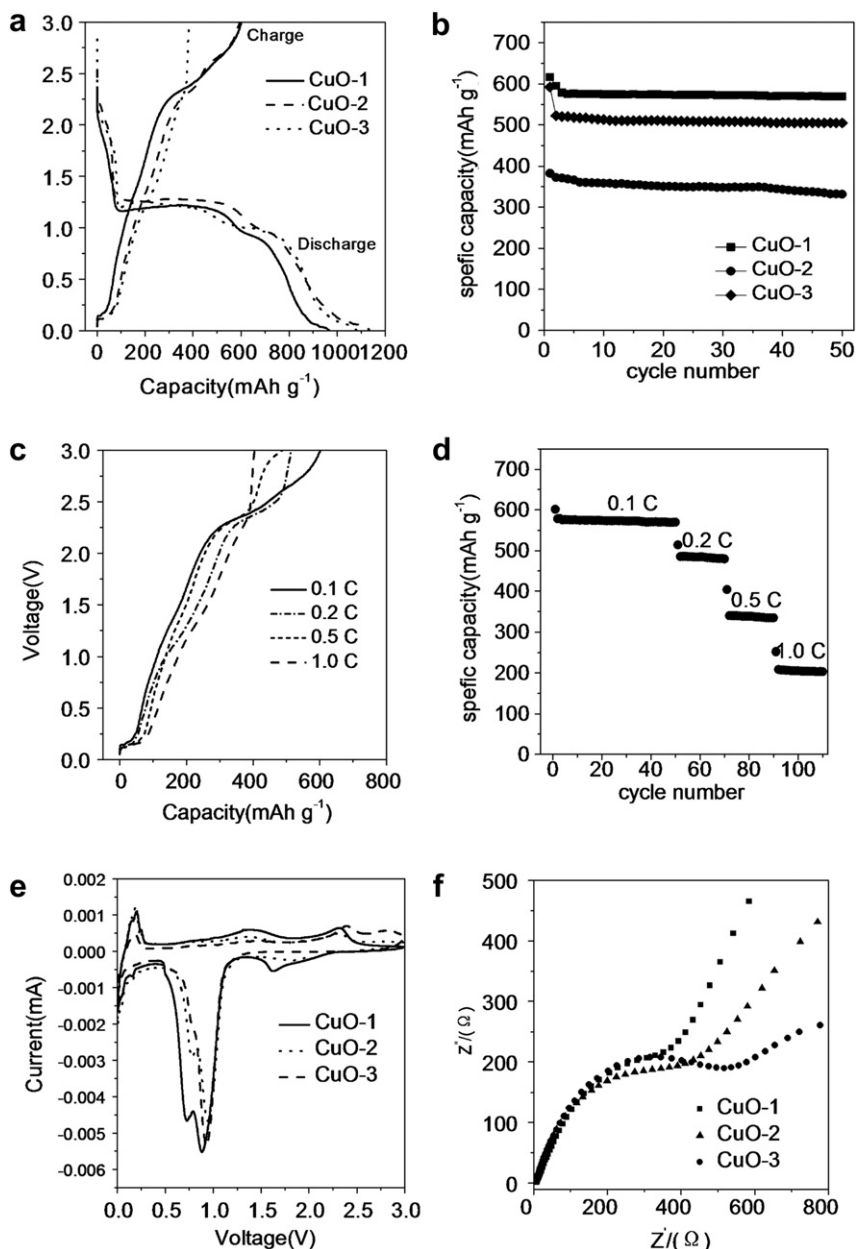
Fig. 6. Electrochemical properties of CuO-1, CuO-2, and CuO-3: (a) initial charge and discharge curves and (b) cycling property between 3.0 and 0.01 V at a current density of 0.1 C, (c) The charge curves and (d) its rate performance of CuO-1 anode at different current densities, (e) CV curves at a scan rate of 0.1 mV s^{-1}, and (f) Nyquist plots at the electrode potentials from 0.70 to 0.10 V.

85.3%, and 86.7% of the initial capacity remained, respectively. This further demonstrates that the mesoporous CuO microspheres with a higher surface area perform better. Although the capacity of mesoporous CuO-1 microspheres obtained here at 0.1 C after 50 cycles is lower than that of hollow CuO microspheres (600 mAh g^{-1} at 0.2 C) [46], and CuO nanorods (650 mAh g^{-1} at 0.5 C) [47], it is much higher than needle-like CuO (441 mAh g^{-1} at 0.1 C) [24], and pillow-shaped porous CuO (320 mAh g^{-1} at 0.1 C) [48]. Fig. 6c reveals that the charge capacities are 514.1, 404.2, and 252.2 mAh g^{-1} at the higher current densities of 0.2, 0.5, and 1.0 C, respectively. The decrease in capacity may be due to electronic conductivity since CuO is a semiconductor [5]. Fig. 6d shows the capacity of CuO-1 after 20 charge/discharge cycles is 479.6 mAh g^{-1} at 0.2 C, 334.8 mAh g^{-1} at 0.5 C, and 203.6 mAh g^{-1} at 1.0 C, further indicating the good cyclability of mesoporous CuO-1 at different scan rates.

Fig. 6e shows the CV curves of a CuO/Li cell at a scan rate of 0.1 mV s^{-1}. In the first discharge process, there are three cathodic peaks for CuO-1, each located at 1.63 V (weak), 0.88 V (strong) and 0.72 V (strong), three cathodic peaks for CuO-2 located at 1.81 V (weak), 0.96 V (strong) and 0.77 V (moderate), two cathodic peaks for CuO-3 located at 0.93 V (strong) and 0.79 V (weak), respectively. These reduction peaks correspond to a multi-step electrochemical reaction that is due to [46,47]: (i) the creation of a solid solution with a CuO phase, (ii) the formation of Cu$_2$O phase, and (iii) the decomposition of Cu$_2$O into Cu and Li$_2$O. Fig. 6f shows the Nyquist plots of mesoporous CuO microspheres. It is well known that the impedance data consisting of one semicircle and a straight line corresponds to the resistance of the Li-ion transfer through the solid electrolyte interphase (SEI) layers in the high frequency range, resistance for charge transfer at the electrode/electrolyte interface in medium-frequency range and the Li-ion Warburg diffusion

Table 2
Physical parameters and electrochemical properties of Cu_2O and CuO samples.

Sample	Average crystal size (nm)	S_{BET} (m^2 g^{-1})	Pore volume (cm^3 g^{-1})	Pore size (nm)	Initial discharge (mAh g^{-1})	Initial charge (mAh g^{-1})	Charge after 50 cycles (mAh g^{-1})
Cu_2O-1	15.0	65.8	0.133	26.7	592.2	430.5	355.2
Cu_2O-2	15.8	45.3	0.114	28.4	575.5	371.1	333.8
Cu_2O-3	20.5	12.7	0.031	~50.0	520.9	280.6	200.6
CuO-1	10.4	37.6	0.102	29.1	967.1	601.6	569.8
CuO-2	12.7	26.5	0.079	31.6	1133.9	592.3	505.1
CuO-3	15.9	5.2	0.024	~50.0	1081.2	382.6	331.7

resistance in the solid electrode material in the low-frequency range [49,50]. It is seen that CuO-1 exhibits smaller semicircles compared with CuO-2 and CuO-3, indicating a lower charge transfer resistance within CuO-1 electrode.

The physical and electrochemical properties of these mesoporous Cu_2O and CuO microspheres are summarized in Table 2. The results show that the mesoporous Cu_2O and CuO microspheres with a higher surface area show a higher capacity and better cyclability than those with a lower surface area because of the smaller crystal size. This is because the porous structure may increase the electronic conductivity [51] of the Cu_2O and CuO electrodes, which will result in a faster electron exchange on the interface of electrolyte/electrode, and a higher reversible capacity and longer cycling life [52,53]. The developed mesoporous structure and high specific surface area can increase the accommodation of lithium ions [54], shorten the diffusion distance for lithium ions [55], reduce charge transfer resistance [56], and increase the absorption of electrolyte [57]. It is well known that highly divided metal oxide particles are able to enhance electrochemical properties via promoting the decomposition of the electrolyte that they contact. In the mesoporous Cu_2O and CuO microspheres, more surface active sites or higher surface to bulk ratio is expected than that in the non-porous Cu_2O and CuO. Therefore, the formation of this SEI layer should become more rapidly detrimental, which is similar to the case of small particles to large one [36]. Nevertheless, their intrinsic kinetic properties still need further investigation.

4. Conclusions

In conclusion, we have comparatively investigated the electrochemical property of mesoporous copper oxide (Cu_2O and CuO) microspheres with different surface areas as anode materials in Li-ion batteries. A facile hydrothermal method was employed to prepare mesoporous Cu_2O microspheres and subsequent oxidation is applied to obtain mesoporous CuO microspheres. The synthesized mesoporous Cu_2O and CuO microspheres with a diameter of 400–1000 nm possess surface area of 12.7–65.8 and 5.2–37.6 m^2 g^{-1} and average crystal size of 15.0–20.5 and 10.4–15.9 nm, respectively. The mesoporous Cu_2O-1 and CuO-1 microspheres with higher surface area show an initial charge capacity of 430.5 mAh g^{-1} and 601.6 mAh g^{-1} and deliver a capacity as high as 355.2 mAh g^{-1} and 569.8 mAh g^{-1} than the Cu_2O and CuO microspheres with lower surface area after 50 cycles, respectively, The charge–discharge experiments and CV reveal that the surface area plays an important role in determining the electrochemical performance of mesoporous Cu_2O and CuO microspheres, as the highly developed mesoporous structure can enhance the accommodation of lithium ions, shorten the diffusion distance for lithium ions, and increase the absorption of electrolyte. We hope that the present study will be beneficial to the development of high capacity and long cycling life anode materials for the next generation of Li-ion cells.

References

[1] P. Bruce, B. Scrosati, J. Tarascon, Angew. Chem. Int. Ed. 47 (2008) 2930–2946.
[2] B. Dunn, H. Kamath, J.M. Tarascon, Science 334 (2011) 928–935.
[3] J. Goodenough, Y. Kim, Chem. Mater. 22 (2010) 587–603.
[4] H. Li, Z. Wang, L. Chen, X. Huang, Adv. Mater. 21 (2009) 4593–4607.
[5] P. Poizot, S. Laruelle, S. Grugeon, L. Dupont, J.M. Tarascon, Nature 407 (2000) 496–499.
[6] M. Wagemaker, W. Borghols, F. Mulder, J. Am. Chem. Soc. 129 (2007) 4323–4327.
[7] M. Armand, J.M. Tarascon, Nature 451 (2008) 652–657.
[8] J.H. Ku, Y.S. Jung, K.T. Lee, C.H. Kim, S.M. Oh, J. Electrochem. Soc. 156 (2009) A688–A693.
[9] X.W. Lou, D. Deng, J.Y. Lee, J. Feng, L.A. Archer, Adv. Mater. 20 (2008) 258–262.
[10] L. Taberna, S. Mitra, P. Poizot, P. Simon, J.M. Tarascon, Nat. Mater. 5 (2006) 567–573.
[11] B. Wang, J.S. Chen, H.B. Wu, Z. Wang, X.W. Lou, J. Am. Chem. Soc. 133 (2011) 17146–17148.
[12] J.S. Chen, Y.L. Cheah, S. Madhavi, X.W. Lou, J. Phys. Chem. C 114 (2010) 8675–8678.
[13] C. Guo, M. Wang, T. Chen, X.W. Lou, C.M. Li, Adv. Energy Mater. 1 (2011) 736–741.
[14] X.H. Wang, Z.B. Yang, X.L. Sun, X.W. Li, D.S. Wang, P. Wang, D.Y. He, J. Mater. Chem. 21 (2011) 9988–9990.
[15] L.J. Fu, J. Gao, T. Zhang, Q. Cao, L.C. Yang, Y.P. Wu, R. Holze, H.Q. Wu, J. Power Sources 174 (2007) 1197–1200.
[16] J. Morales, L. Sanchez, F. Martin, J. Ramosbarrado, M. Sanchez, Thin Solid Films 474 (2005) 133–140.
[17] Z. Lin, W. Yue, D. Huang, J. Hu, X. Zhang, Z. Yuan, X. Yang, RSC Adv. 2 (2012) 1794–1797.
[18] K.M. Shaju, F. Jiao, A. Debart, P.G. Bruce, Phys. Chem. Chem. Phys. 9 (2007) 1837–1842.
[19] S. Xiong, J.S. Chen, X.W. Lou, H.C. Zeng, Adv. Funct. Mater. 22 (2011) 861–871.
[20] Y. Ren, A.R. Armstrong, F. Jiao, P.G. Bruce, J. Am. Chem. Soc. 132 (2010) 996–1004.
[21] F.F. Cao, X.L. Wu, S. Xin, Y.G. Guo, L.J. Wan, J. Phys. Chem. C 114 (2010) 10308–10313.
[22] J. Lee, Y.S. Jung, S.C. Warren, M. Kamperman, S.M. Oh, F.J. DiSalvo, U. Wiesner, Macromol. Chem. Phys. 212 (2011) 383–390.
[23] X. Guan, L. Li, G. Li, Z. Fu, J. Zheng, T. Yan, J. Alloys Compd. 509 (2011) 3367–3374.
[24] J.Y. Xiang, J.P. Tu, L. Zhang, Y. Zhou, X.L. Wang, S.J. Shi, J. Power Sources 195 (2010) 313–319.
[25] F. Ke, L. Huang, G. Wei, L. Xue, J. Li, B. Zhang, S. Chen, X. Fan, S. Sun, Electrochim. Acta 54 (2009) 5825–5829.
[26] J.Y. Xiang, J.P. Tu, L. Zhang, Y. Zhou, X.L. Wang, S.J. Shi, Electrochim. Acta 55 (2010) 1820–1824.
[27] W. Zhang, M. Li, Q. Wang, G. Chen, M. Kong, Z. Yang, S. Mann, Adv. Funct. Mater. 21 (2011) 3516–3523.
[28] T.E. García, M. Valvo, U. Lafont, C. Locati, D. Munao, E.M. Kelder, J. Power Sources 196 (2011) 6425–6432.
[29] Y.J. Mai, X.L. Wang, J.Y. Xiang, Y.Q. Qiao, D. Zhang, C.D. Gu, J.P. Tu, Electrochim. Acta 56 (2011) 2306–2311.
[30] S. Bijani, M. Gabas, L. Martinez, J. Ramosbarrado, J. Morales, L. Sanchez, Thin Solid Films 515 (2007) 5505–5511.
[31] C.Q. Zhang, J.P. Tu, X.H. Huang, Y.F. Yuan, X.T. Chen, F. Mao, J. Alloys Compd. 441 (2007) 52–56.

[32] X. Lin, R. Zhou, J. Zhang, S. Fei, Appl. Surf. Sci. 256 (2009) 889–893.
[33] L.J. Fu, J. Gao, T. Zhang, Q. Cao, L.C. Yang, Y.P. Wu, R. Holze, J. Power Sources 171 (2007) 904–907.
[34] S. Grugeon, S. Laruelle, R. Herrera-Urbina, L. Dupont, P. Poizot, J.M. Tarascon, J. Electrochem. Soc. 148 (2001) A285–A292.
[35] Z. Zhang, H. Che, Y. Wang, J. Gao, L. Zhao, X. She, J. Sun, P. Gunawan, Z. Zhong, F. Su, Ind. Eng. Chem. Res. 51 (2012) 1264–1274.
[36] P. Poizot, S. Laruelle, S. Grugeon, L. Dupont, J.M. Tarascon, J. Power Sources 97–98 (2001) 235–239.
[37] Y. Luo, S. Li, Q. Ren, J. Liu, L. Xing, Y. Wang, Y. Yu, Z. Jia, J. Li, Cryst. Growth Des. 7 (2007) 87–92.
[38] X.D. Liang, L. Gao, S.W. Yang, J. Sun, Adv. Mater. 21 (2009) 2068–2071.
[39] L.A. Gao, B.P. Ha, J. Cryst. Growth 303 (2007) 616–621.
[40] L. Yang, M. Takahashi, B.F. Wang, Electrochim. Acta 51 (2006) 3228–3234.
[41] J.Y. Xiang, X.L. Wang, X.H. Xia, L. Zhang, Y. Zhou, S.J. Shi, J.P. Tu, Electrochim. Acta 55 (2010) 4921–4925.
[42] J. Jamnik, R. Dominko, B. Erjavec, M. Remskar, A. Pintar, M. Gaberscek, Adv. Mater. 21 (2009) 2715–2719.
[43] Y.S. Hu, Y.G. Guo, W. Sigle, S. Hore, P. Balaya, J. Maier, Nat. Mater. 5 (2006) 713–717.
[44] Y. Lee, I. Leu, S. Chang, C. Liao, K. Fung, Electrochim. Acta 50 (2004) 553–559.
[45] Z.H. Yang, H.Q. Wu, Solid State Ionics 143 (2001) 173–180.
[46] S.Q. Wang, J.Y. Zhang, C.H. Chen, Scr. Mater. 57 (2007) 337–340.
[47] Z. Wang, F. Su, S. Madhavi, X.W. Lou, Nanoscale 3 (2011) 1618–1623.
[48] M. Wan, D. Jin, R. Feng, L. Si, M. Gao, L. Yue, Inorg. Chem. Commun. 14 (2011) 38–41.
[49] N. Sharma, J. Plevert, G.V.S. Rao, B.V.R. Chowdari, T.J. White, Chem. Mater. 17 (2005) 4700–4710.
[50] M.V. Reddy, S. Madhavi, G.V.S. Rao, B.V.R. Chowdari, J. Power Sources 162 (2006) 1312–1321.
[51] A. Latz, J. Zausch, J. Power Sources 196 (2011) 3296–3302.
[52] C.Y. Yu, Z.L. Wang, Y. Chen, D.G. Xia, W.S. Chu, Z.Y. Wu, Rare Met. 28 (2009) 317–321.
[53] H.P. Zhao, C.Y. Jiang, X.M. He, J.G. Ren, C.R. Wan, Ionics 14 (2008) 113–120.
[54] H. Nara, Y. Fukuhara, A. Takai, M. Komatsu, H. Mukaibo, Y. Yamauchi, T. Momma, K. Kuroda, T. Osaka, Chem. Lett. 37 (2008) 142–143.
[55] J.K. Feng, H. Xia, M.O. Lai, L. Lu, Mater. Res. Bull. 46 (2011) 424–427.
[56] Y.J. Mai, J.P. Tu, X.H. Xia, C.D. Gu, X.L. Wang, J. Power Sources 196 (2011) 6388–6393.
[57] M.M. Rahman, J.Z. Wang, M.F. Hassan, Z.X. Chen, H.K. Liu, J. Alloy. Compd. 509 (2011) 5408–5413.